

Experimental neuromorphic computing based on quantum memristor

Mirela Selimović,^{1,2} Iris Agresti,³ Michał Siemaszko,⁴ Joshua Morris,^{1,2} Borivoje Dakić,^{1,5,6} Riccardo Albiero,⁷ Andrea Crespi,⁸ Francesco Ceccarelli,⁷ Roberto Osellame,⁷ Magdalena Stobińska,⁴ and Philip Walther^{1,5,6}

¹*University of Vienna, Faculty of Physics, Vienna Center for Quantum Science and Technology (VCQ), Boltzmannngasse 5, Vienna 1090, Austria*

²*Vienna Doctoral School in Physics (VDSP), Boltzmannngasse 5, 1090 Vienna, Austria*

³*University of Vienna, Faculty of Physics, Quantum Science and Technology (VCQ), Boltzmannngasse 5, Vienna 1090, Austria*

⁴*Faculty of Mathematics, Informatics, and Mechanics,*

University of Warsaw, Stefana Banacha 2, 02-097 Warsaw, Poland

⁵*Institute for Quantum Optics and Quantum Information Sciences (IQOQI), Austrian Academy of Sciences, Boltzmannngasse 3, Vienna 1090, Austria*

⁶*QUBO Technology GmbH, 1090 Vienna, Austria*

⁷*Istituto di Fotonica e Nanotecnologie, Consiglio Nazionale delle*

Ricerche (IFN-CNR), piazza L. Da Vinci 32, 20133 Milano, Italy

⁸*Dipartimento di Fisica, Politecnico di Milano, piazza L. da Vinci 32, 20133 Milano, Italy*

Machine learning has recently developed novel approaches, mimicking the synapses of the human brain to achieve similarly efficient learning strategies. Such an approach retains the universality of standard methods, while attempting to circumvent the excessive requirements, which hinder their scalability. In this context, quantum (or quantum inspired) algorithms may bring further enhancement. However, high-performing neural networks invariably display non-linear behaviours, which is diametrically opposed to the linear evolution of closed quantum systems. We propose a solution to this issue and report the first neuromorphic architecture based on a photonic quantum memristor. In detail, we show how the memristive feedback loop enhances the non-linearity and hence the performance of the algorithm. We benchmark our model on two tasks, i.e. non-linear function and time series prediction. In these cases, we highlight the essential role of the quantum memristive element and demonstrate the possibility of using it as a building block in more sophisticated networks.

I. INTRODUCTION

In the last decades, machine learning has fundamentally changed the approach to solving a wide variety of problems, from everyday life to scientific scopes [1–7]. In this context, artificial neural networks (ANN) have proven to be a pivotal tool, especially for tackling tasks where information needs to be extracted from high-dimensional data [8]. Nevertheless, a growing number of parameters must be trained, with correspondingly larger training data, as the tasks get more complex, resulting in the so-called memory bottleneck [9]. This sparked the development of more dedicated hardware, i.e. neuromorphic architectures, which mimic the human brain [10]. The main advantage of these models is their minimal learning requirements, which circumvents the aforementioned difficulty. Acting as the poster-child of neuromorphic components is the memristor, a passive circuitual component that was postulated in 1971 [11] and demonstrated in 2008 [12]. Its main characteristic is that it retains memory of its past states, in the form of a hysteresis that is similar to neural synapses [10, 13–16].

A related but somewhat orthogonal paradigm shift in computer science was introduced by quantum computing. The interest in this field stems, first, from the possibility of tackling non-classical processing tasks directly related to the investigation of quantum effects and, second, from the promise of outperforming standard algorithms for particular problems [18–21]. However, for the latter, the only proven advantages were shown either for tasks which

are out of reach of even near term state-of-the-art quantum computers or which have no known applications [22]. Hence, a research line that has attracted a lot of interest arises from the combination of machine learning and quantum computation, i.e. Quantum Machine Learning (QML) [23, 24]. This is fueled by the hope that a computational advantage can be found on practically relevant tasks even when using relatively small scale quantum information processing. Furthermore, photonic apparatuses exhibit vastly lower energy consumption, compared to standard electrical ones [25, 26], indicating the possibility of far more efficient computational platforms. However, in this context, the main difficulty lies in the deterministic implementation of non-linear operations (crucial for the learning process, see Fig. 1a), since the evolution of closed quantum systems is intrinsically unitary (and therefore linear). Moreover, the introduction of interactions with the environment results in the reduction of the coherence of the overall system which, in turn, leads to a processing power that approaches the one of classical information processing. This is the reason for which employing Fock states for QML algorithms is challenging, although they can grant enhanced expressivity and they allow reaching higher-dimensional Hilbert spaces [27–29] with respect to (weakly)-coherent light inputs [30–33].

In this work, we propose a solution to this apparent conundrum and we implement the first instances of a neuromorphic computing protocol, i.e. reservoir computing (RC), on a photonic platform. We achieve this by exploiting single photon states manipulated through

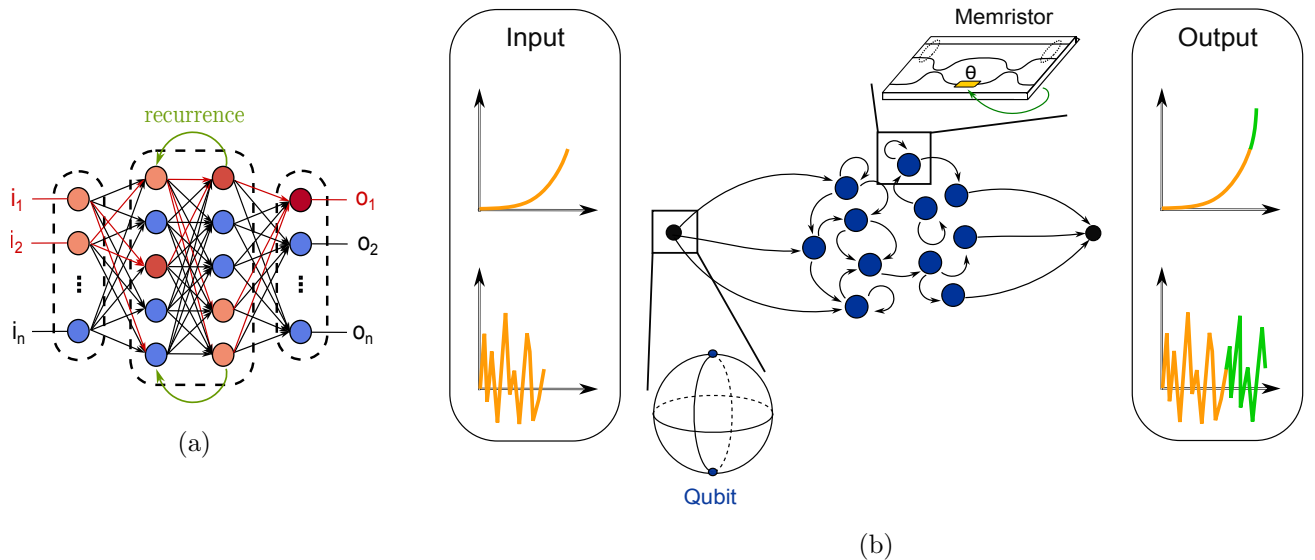


FIG. 1: **Neuromorphic computing based on quantum memristor.** (a) Non-linear activation functions in neural networks are crucial for learning input/output correlations. Indeed, linear functions limit the expressiveness of the model, not allowing for nuanced decisions. (b) The basic principle of a quantum memristor is a tunable Mach-Zehnder interferometer, where its internal phase (θ) is varied, according to the output registered at one of its output modes, through a feedback loop. The investigated hybrid quantum/classical models are implemented through three parts: input encoding (quantum), non-linear reservoir (quantum) and one-layered ANN (classical). In our work, the encoding of classical variables in a one qubit state exploits the amplitude of the component parallel to $|0\rangle$, i.e. $x \rightarrow \sqrt{x}|0\rangle + \sqrt{1-x}|1\rangle$ and $x|0\rangle + \sqrt{1-x^2}|1\rangle$. The reservoir consists in a unitary operation, composed by the product of different rotations. These rotations allow us to achieve a non-linear transformation of the input, due to the encoding that is non-linear in the density matrix of the quantum state. The loop enhances the achievable non-linearity, while implementing a short-term memory. The non-linear reservoir is then followed by a classical ANN, which is the only part of the model that is trained, producing a weighted sum of the reservoir outputs. The two addressed tasks are the prediction of a smooth non-linear function and of a random time series.

an integrated circuit [34]. The model may be seen as a building block for more complex networks and is composed of a non-linear fixed reservoir (equipped with classical memory), followed by a one-layered linear ANN, which is the only part that requires a training phase (see Fig. 1b). Our aim is to implement a quantum/classical hybrid algorithm, where the non-linear element is generated by a quantum system, while the ANN is classical. To achieve this goal we leverage a particular choice for the input encoding and the exploitation of a novel device: the photonic quantum memristor [35]. This element has the two-fold effect of enhancing the non-linearity of the model, while implementing a classical memory. Such a device is based on a Mach-Zehnder interferometer equipped with a feedback loop, and its behaviour is proven to be *memristive*. However, its potential use for machine learning tasks was only theorized and its role was not deeply investigated, as the studied task, the recognition of MNIST hand-written digits [36], can be tackled effectively through linear regression and other simple estimators. Here, we go beyond the previous study and apply this hardware to two machine-learning tasks where non-linearity is a crucial factor and cannot be omitted without compromising performance,

highlighting the pivotal role of the quantum reservoir. In both of the considered tasks, we show that the dynamics of the photonic quantum memristor enhances the performance, with respect to the case where no feedback loop is implemented. Hence, the present work shows how a (photonic) quantum system can tackle tasks that were addressed with similar classical architectures [14], but with substantially less resources, paving the way to resource efficient machine learning models and to the possibility of exploring neuromorphic architectures applied to quantum tasks.

II. QUANTUM MEMRISTOR-BASED NEUROMORPHIC MODELS

The photonic quantum memristor can be modeled as a tunable Mach-Zehnder interferometer, as depicted in Fig. 2. Then, its internal phase is updated according to a feedback rule that depends on the measurement outcome at one output mode, affecting the temporal dynamics of the device. One of its main features consists in the fact that, when tracing out the mode used for the feedback loop, the remaining reduced state may still be partially

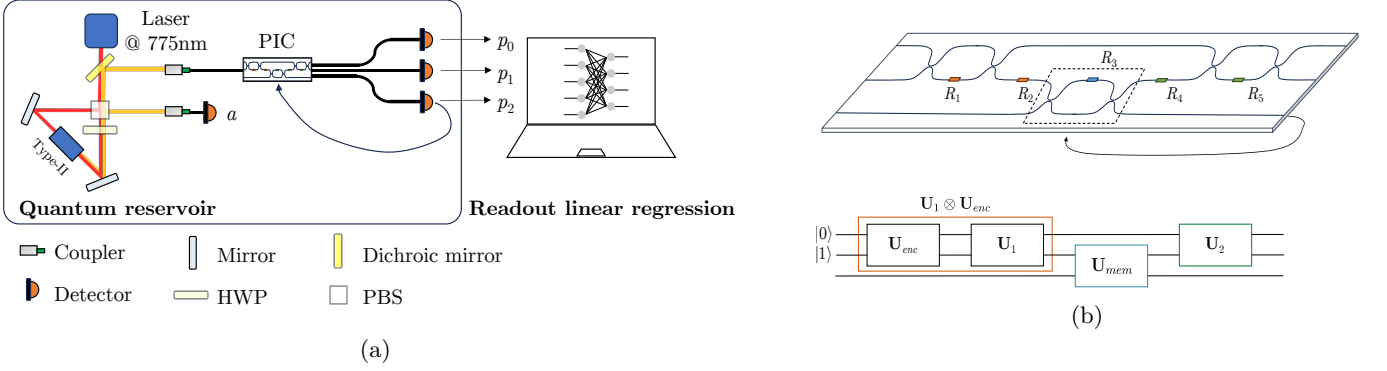


FIG. 2: Experimental setup. (a) The experimental apparatus consists of a source of single photon pairs, which is pumped with a laser at 775 nm and generates degenerate photon pairs at 1550 nm. One photon is routed to the 3 input/output mode photonic integrated circuit (PIC) and the other photon is ancillary. Let us note that this circuit is implemented following the universal Reck architecture [17]. At the outputs of the PIC, photon counts are registered by superconducting nanowire single photon detectors. After the full calibration of the chip, phases are set and modulated by applying a suitable voltage to the resistive elements, that act as thermal phase shifters. The unitary operation is updated, conditioned on the statistics of previous runs. The output distribution is then fed into a classical ANN, which is the only part of the machine learning model that is trained. (b) The PIC consists in 3 Mach-Zehnder interferometers and 5 tunable phases. The R_i indicate the resistive elements that serve as tunable thermal phase shifters, where R_3 is updated conditioned on the output of the third mode, implementing a memristive behaviour. Let us note that the state obtained tracing out the third output still preserves coherence (see section II of the Supplemental Material). The input is encoded in one qubit, through a unitary transformation \mathbf{U}_{enc} . The unitary transformations \mathbf{U}_1 and \mathbf{U}_2 are hyperparameters of our model. Then, \mathbf{U}_{mem} amounts to the action of the memristor and is varied depending on previous outcomes. Also the feedback rule, according to which this happens, is a hyperparameter.

coherent relative to the joint state, as detailed in section II of the Supplementary Material. Consequently, further quantum information processing is possible on the output.

We want to exploit this feedback mechanism to implement non-linear operations on the input state and utilize a short-term memory, to achieve a proof-of-principle quantum reservoir computing (QRC). In detail, we encode our classical inputs in quantum states that are then injected into a quantum reservoir. This usually consists of randomly connected nodes, whose internal time-based state make up its intrinsic memory and the historical non-linearity that is necessary for the learning process (see the section I of the Supplemental Material for further details). In our implementation, one physical node realized through a Mach-Zehnder interferometer (MZI), which in concert with a feedback loop acts like a quantum memristor. Then, the randomness is given by unitary operations before and after the memristor itself. Hence, the quantum part of our model consists in the encoding of the classical data and reservoir. In particular, we exploit one-qubit states, encoded in the path degree of freedom of a single photon state, with a dual-rail scheme (see Fig. 2b). The reservoir is then composed of a sequence of three unitaries over three spatial modes, i.e. \mathbf{U}_1 , \mathbf{U}_{mem} and \mathbf{U}_2 . At the end, to build a proper reservoir computing scheme, a single trainable feedforward neural network follows.

We test our model for two tasks, that rely on the two key features of our photonic platform, i.e. non-linearity and short-term memory. These are a non-linear function prediction/reproduction, where we exploit mostly the non-linearity of the model, and a time series prediction (*Non-linear Auto Regressive Moving Average* [37, 38]), where short-term memory plays a pivotal role.

For the first task, the functions we aim at reproducing and then extrapolating are monomials:

$$f(x) = x^n, \quad n \in \mathbb{Z} \quad (1)$$

this choice is motivated by the interest in practically testing the maximal achievable non-linear behaviour of our model and the role of the feedback loop towards its enhancement.

We encode the inputs as follows: $x \rightarrow \sqrt{x}|0\rangle + \sqrt{1-x}|1\rangle$. Note that this encoding is linear when performing a projective measurement in the eigenbasis of the Pauli operator σ_Z [39], as $\text{Tr}(\sigma_Z \rho_x) = \sum_{i=0,1} (-1)^i p_i = 2x - 1$, where p_i is the probability of getting the outcome i . In contrast, measurements in the σ_X basis give an expectation value that is non-linear in x , $\text{Tr}(\sigma_X \rho_x) = \sqrt{x}\sqrt{1-x}$. This non-linearity can be enhanced by a proper choice of the rotations \mathbf{U}_1 and \mathbf{U}_2 . Then, we pick a linear feedback rule which modifies \mathbf{U}_{mem} . In particular, the internal variable of the memristor R_t , which can be seen as the reflectivity of a beam-splitter, is updated via:

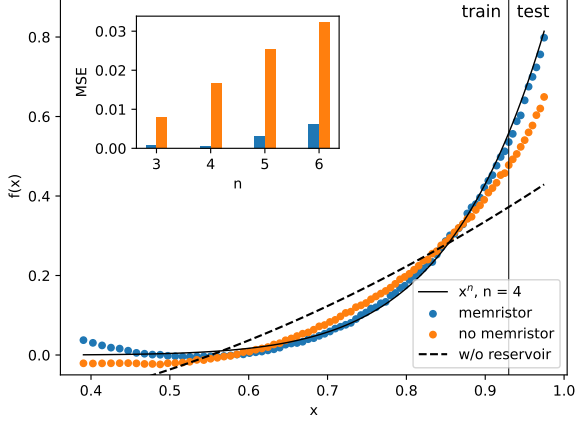


FIG. 3: **Non-linear function prediction results.**

The blue dots show the experimental results for the prediction of the power function $f_t(x) = x^n$ for $n = 4$ (indicated by the solid black curve). The orange ones show the results for the same task, but without feedback loop. Inputs lower than 0.9 are used for training the model, while the other ones are used for test. The case with no feedback loop is on average 34% less accurate than the one exploiting the memristor. Let us note that, to have a fair comparison, hyperparameter were optimized separately for the two cases. The dashed black line represents the case without the physical reservoir, i.e. where the inputs x are directly injected to the ANN. The loss function is defined as the mean squared error MSE between the target function $f_t(x) = y_t$ and the test data y_{test}^k , i.e. $y_t - y_{test}$. The inset shows the MSE for power function with $n = 3, 4, 5, 6$ in the QRC case (blue) and with no feedback loop case (orange).

$$R_t = \frac{1}{m} \sum_{T=t-m}^t R_T = \frac{1}{m} \sum_{T=t-m}^t (ap_{2T} + b) \quad (2)$$

where m is the *memory extent*, p_{2T} is the probability of detecting a photon in the update mode and the internal phase of the MZI implementing \mathbf{U}_{mem} is given by $2 \times \arccos(\sqrt{R})$. The rotations \mathbf{U}_1 and \mathbf{U}_2 , along with a and b , are optimizable hyperparameters (see section IA of the Supplementary Material for further details).

The goal of the second task is to predict the output of a non-linear dynamical system, introduced in [37, 38], called *NARMA*. This was already widely used as a benchmark for classical [40, 41] and quantum [42, 43] RC models. The recurrence relation of the system is described by the following equation:

$$y_{k+1} = 0.4y_k + 0.4y_k y_{k-1} + 0.6x_k^3 + 0.1, \quad (3)$$

where x_k and y_k is the input and the output, respectively, at time k .

From Eq. (3), it is visible that the output y_{k+1} depends on past two outputs y_k and y_{k-1} .

The time series $\mathbf{x} = \{x_i\}_{i=1}^N$ is generated by sampling each x_i independently and uniformly in the interval $U(0, \frac{1}{2})$, and then outputs $\mathbf{y} = \{y_i\}_{i=1}^N$ come sequentially from Eq. (3). For this task, we are using the amplitude encoding $x_i \mapsto x_i |0\rangle + \sqrt{1 - x_i^2} |1\rangle$ and the feedback rule

$$R_t = R_{t-1} + \frac{p_{(t-1)2} - R_{t-1}}{m}, \quad (4)$$

where p_{ti} is the probability of detecting one photon in the i -th mode ($i = 0, 1, 2$), at time t , while m is the fixed *memory extent* of the memristor (see section IB of the Supplementary Material for further details).

For both tasks, the collected experimental statistics are fed into the classical readout ANN that is trained to perform the given task.

As a benchmark, we performed the task also without any feedback loop and with no reservoir. The latter is a fully classical procedure, only injecting the x values into the final ANN, to highlight the role of our physical platform.

III. EXPERIMENTAL IMPLEMENTATION

The main part of the experimental setup, fully represented in Fig. 2, is the physical quantum reservoir for information processing. It consists of an integrated waveguide circuit with 3 input/output modes and is designed according to a universal architecture [44]. The waveguides are fabricated by direct femtosecond laser writing [35, 45, 46] in an alumino-borosilicate glass substrate and feature single-mode operation at 1550 nm. Microstructured thermo-optic phase shifters are integrated on-chip, to provide efficient phase tunability [47]. Input and output ports are pigtailed with single-mode fibers.

The encoding of the classical input is set via an initial unitary transformation \mathbf{U}_{enc} , through an on-chip MZI, as shown in Fig. 1b. For example, to encode the state $\sqrt{x}|0\rangle + \sqrt{1-x}|1\rangle$, apply a phase $\phi = 2 \arccos(x)$ when injecting a photon into the lower mode of the MZI. However, since the PIC consists of three MZIs in total, we implement the product $\mathbf{U}_1 \cdot \mathbf{U}_{enc}$ through the first MZI, as detailed in Fig. 2b.

The input single photon state is generated by a collinear Type-II spontaneous parametric down conversion source, pumped at 775 nm, which emits pairs of degenerate photons with a wavelength of 1550 nm. The employed non-linear crystal is a periodically poled titanyl phosphate, placed within a Sagnac interferometer. Since for this application we do not need entangled states, the crystal is pumped only in one spatial direction and generates the separable state $|01\rangle$. One photon is ancillary and heralds the generation of the second photon that is injected into the photonic processor. The three output modes of the photonic processor are connected to superconducting nanowire single photon detectors.

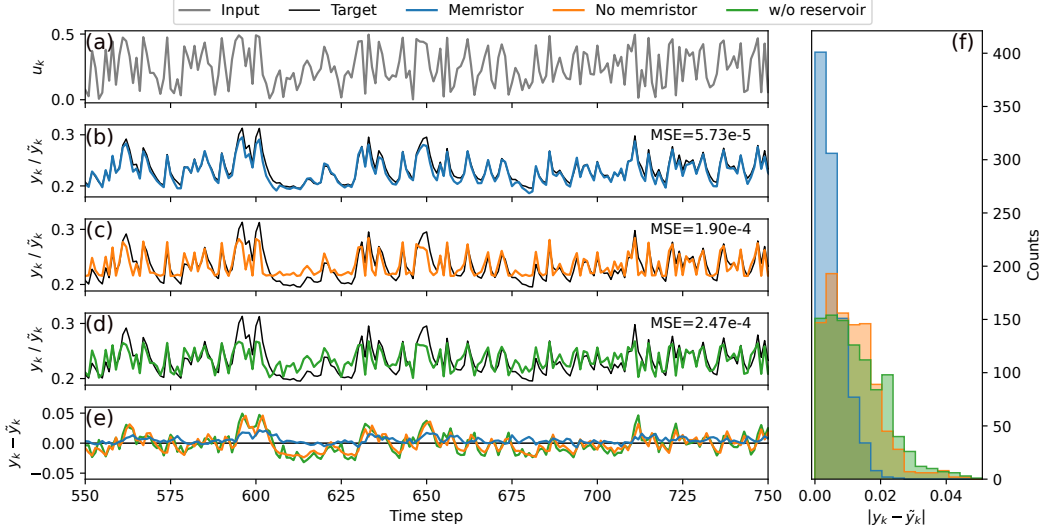


FIG. 4: **NARMA task results.** (a) Sequence of inputs of the NARMA function, which are generated by sampling each x independently from a uniform distribution between 0 and $\frac{1}{2}$. (b)-(d) Sequence of outputs y (black), evaluated according to Eq. (3), together with the experimental prediction of our memristor-based model (blue); with no feedback loop (orange) and no reservoir (green). (e) Absolute difference between the true and predicted output. The adopted dataset contains 1000 points. Out of those, the first 20 correspond to the so-called *washout*, i.e. the time required to the model to be properly initialized, the training process is done on the following 480 points and then the validation is performed on the rest of the dataset. However, for the sake of clarity, the plot shows only 200 points of the test. The corresponding MSE are 5.73×10^{-5} , 1.90×10^{-4} and 2.47×10^{-4} . (f) Histogram displaying the absolute differences between true and predicted outputs (respectively in blue, orange and green).

At this point, the frequencies of the clicks registered by the three detectors at the output of the chip, in coincidence with the one detecting the heralding photon, give the probabilities p_0 , p_1 and p_2 as $p_i = \frac{N_{i,a}}{\sum_{j=1}^3 N_{j,a}}$.

IV. RESULTS

To quantify the quality of the performance of predictive tasks, we use the so-called *mean squared error* [48], defined as follows:

$$MSE(\mathbf{y}, \tilde{\mathbf{y}}) := \frac{1}{N} \sum_{t=1}^N (y_t - \tilde{y}_t)^2 \quad (5)$$

with y_t target values, \tilde{y}_t predicted values and N data points.

For the function prediction task three different cases are compared: (i) with quantum memristor, (ii) without memory (with no feedback loop) and (iii) with no reservoir. The prediction of x^n with $n = 4$ is shown in Fig. 3 and the inset plot shows the loss function of the readout unit for different n . Note that even without the feedback loop some non-linearity can be generated, due to the encoding from x to ρ_x . However, the feedback loop enhances the impact of the non-linear measurement process and ultimately the performance of the algorithm. On the contrary, in the case of no reservoir, the output is

MODEL	EQUATION	MSE ($\times 10^{-4}$)
L	$y_t \approx \alpha u_t + \beta$	2.76(29)
Q	$y_t \approx \alpha u_t^2 + \beta u_t + \gamma$	2.05(22)
$L + M$	$y_t \approx \alpha u_t + \beta u_{t-1} + \gamma$	1.83(19)
$Q + M$	$y_t \approx \alpha u_t^2 + \beta u_{t-1} + \gamma$	1.22(14)
L^M	$y_t \approx \alpha u_t + \beta \text{Exp}_4(u_t) + \gamma$	1.14(11)
Q^M	$y_t \approx \alpha u_t^2 + \beta \text{Exp}_4(u_t) + \gamma$	0.78(8)
QMEM	-	0.33(8)

TABLE I: **Mean Squared Errors for classical machine learning models.** This table shows the average MSE achieved by several classical models, in comparison to the one presented in this work, indicated by QMEM. The numbers in the bracket indicate one standard deviation of 100 runs. In detail, L and Q stand, respectively, for models that can base their predictions on linear and quadratic manipulation of the input. $L + M$ ($Q + M$) indicates the same models, but with access to the previous element of the output series. In L^M (Q^M), instead, the access to previous elements is extended to the exponential moving average of all the past outputs, with a memory extent of 4. The reported values are obtained through numerical simulations.

simply a linear function, as the final ANN may only act linearly on the input.

In Fig. 4, we show the experimental prediction of the

network for the previously described NARMA task. For the case with no feedback loop, each output depends only on the last input, since only the feedback loop allows storing the information of previous data points. It is noteworthy that the case with no feedback loop still has decent performance, due to the low non-linearity of the task (see section IC of the Supplemental Material for further details). To have a more complete overview of the performance of our algorithm, we compared it with similar classical algorithms. In particular, we tested the aforementioned tasks with models that could base their predictions on a linear or quadratic manipulation of the inputs in three cases: with no memory, with access to the previous outcome and to the exponential moving average of all past inputs, with memory extent equal to 4. For all these cases, the average MSE obtained in our case is lower, highlighting the enhancement brought by the quantum memristor (the numerical values are reported in Table I).

V. DISCUSSION

In this work, we have implemented the first instance of QRC exploiting single photon states based on a quantum memristor device. These machine learning models work by injecting input data into a fixed random reservoir, which is then followed by a one-layered linear ANN (the only part of the model which is trained) [34]. The required non-linearity is provided by the evolution of the quantum system through the photonic quantum memristor.

The last part of the model, featuring an ANN, is implemented through standard computing. We tested our model on two function prediction tasks: several power functions and the NARMA task. Due to its regularity, the first case is only to test the non-linearity that is achievable through our apparatus. The latter instead tests also the memory of our model, given that its outcomes depend on previous ones.

Ours is the first example of neuromorphic architectures exploiting single-photon states (encoded in the path degree of freedom) and implementing a non-linear behaviour through an adaptive protocol, performed by the quantum memristor. Moreover, we carry out a systematic analysis to distinguish the source of such a non-linearity, i.e. the encoding or the feedback loop. For this reason, for all of the tasks, we compare the case featur-

ing the quantum memristor (QRC), to the case without feedback loop. For all of the cases, the quantum memristor brings an enhanced accuracy with respect to classical models. This scheme, although applied to relatively simple tasks, can be seen as a building block for more complex networks, as the output of the memristor, tracing out the update mode, preserves coherence and can be used as an input for successive layers (see section II of the Supplemental Material for further details).

This study paves the way for further investigations related to the non-linearities achievable on photonic platforms. This is particularly relevant, considering that hybrid optical-electronic ANNs have been proven to require a lower energy consumption than standard ones [25, 26].

In this framework, the memristor could be employed to constitute the activation function layer of quantum neural networks. Another interesting feature is that a quantum reservoir could be used to directly process quantum systems, tackling tasks with no classical equivalent. For instance, to investigate foundational aspects or quantum state properties [49–51]. Further studies can involve the implementation of a quantum feedback, where previous states interfere with new ones, through a loop architecture [52]. Analogously, the implementation of a fast feedback would allow to make coherent adjustments to the quantum state. This would allow for a larger memory storage and open up to the possibility of tackling a wider range of tasks.

ACKNOWLEDGMENTS

The fabrication of the photonic integrated circuit was partially carried out at PoliFAB (<https://www.polifab.polimi.it/>), the micro- and nano-fabrication facility of Politecnico di Milano. F.C. and R.O. would like to thank the PoliFAB staff for technical advice and support. This research was funded in whole or in part by the Austrian Science Fund (FWF)[10.55776/ESP205] (PREQUrSOR), [10.55776/F71] (BeyondC), [10.55776/FG5] (Research Group 5) and [10.55776/I6002] (PhoMemtor).

COMPETING INTERESTS

The authors declare no competing interest.

-
- [1] Abdel-Hamid, O. *et al.* Convolutional neural networks for speech recognition. *IEEE Transactions on Audio, Speech and Language Processing* **22**, 1533–1545 (2014). Publisher: Institute of Electrical and Electronics Engineers Inc.
 - [2] Bakator, M. & Radosav, D. Deep learning and medical diagnosis: A review of literature. *Multimodal Technolo-*

gies and Interaction **2** (2018).

- [3] Silver, D. *et al.* Mastering the game of Go without human knowledge. *Nature* **550**, 354–359 (2017).
- [4] Pierson, H. A. & Gashler, M. S. Deep learning in robotics: a review of recent research. *Advanced Robotics* **31**, 821–835 (2017).

- [5] Hsu, F.-H. Ibm’s deep blue chess grandmaster chips. *IEEE Micro* **19**, 70–81 (1999).
- [6] Jumper, J. *et al.* Highly accurate protein structure prediction with AlphaFold. *Nature* **596**, 583–589 (2021).
- [7] Brown, T. B. *et al.* Language Models are Few-Shot Learners. *arXiv preprint arXiv:2005.14165v4* (2020).
- [8] Krizhevsky, A., Sutskever, I. & Hinton, G. E. ImageNet classification with deep convolutional neural networks. *Communications of the ACM* **60**, 84–90 (2017).
- [9] Mutlu, O., Ghose, S., Gómez-Luna, J. & Ausavarungrun, R. Processing data where it makes sense: Enabling in-memory computation. *Microprocessors and Microsystems* **67**, 28–41 (2019). 1903.03988.
- [10] Ham, D., Park, H., Hwang, S. & Kim, K. Neuromorphic electronics based on copying and pasting the brain. *Nat Electron* **4**, 635–644 (2021).
- [11] Chua, L. Memristor-the missing circuit element. *IEEE Transactions on Circuit Theory* **18**, 507–519 (1971).
- [12] Strukov, D. B., Snider, G. S., Stewart, D. R. & Williams, R. S. The missing memristor found. *Nature* **453**, 80–83.
- [13] Jo, S. H. *et al.* Nanoscale memristor device as synapse in neuromorphic systems. *Nano Lett.* **10**, 1297–1301 (2010).
- [14] Du, C. *et al.* Reservoir computing using dynamic memristors for temporal information processing. *Nature Communications* **8**, 2204 (2017).
- [15] Xiao, Y. *et al.* A review of memristor: material and structure design, device performance, applications and prospects. *Science and Technology of Advanced Materials* **24**, 2162323 (2023).
- [16] Zhong, Y. *et al.* Dynamic memristor-based reservoir computing for high-efficiency temporal signal processing. *Nature communications* **12**, 408 (2021).
- [17] Reck, M., Zeilinger, A., Bernstein, H. J. & Bertani, P. Experimental realization of any discrete unitary operator. *Physical Review Letters* **73**, 58–61 (1994).
- [18] Grover, L. K. A fast quantum mechanical algorithm for database search. In *Proceedings of the Twenty-Eighth Annual ACM Symposium on Theory of Computing*, STOC ’96, 212–219 (Association for Computing Machinery, New York, NY, USA, 1996).
- [19] Shor, P. W. Polynomial-time algorithms for prime factorization and discrete logarithms on a quantum computer. *SIAM Review* **41** (1999).
- [20] Montanaro, A. Quantum algorithms: An overview. *npj Quantum Information* **2** (2016). 1511.04206.
- [21] Harrow, A. W., Hassidim, A. & Lloyd, S. Quantum Algorithm for Linear Systems of Equations. *Physical Review Letters* **103**, 150502 (2009).
- [22] Arute, F. *et al.* Quantum supremacy using a programmable superconducting processor. *Nature* **574**, 505–510.
- [23] Dunjko, V. & Briegel, H. J. Machine learning & artificial intelligence in the quantum domain: a review of recent progress. *Reports on Progress in Physics* **81**, 074001 (2018).
- [24] Wittek, P. *Quantum machine learning: what quantum computing means to data mining* (Academic Press, 2014).
- [25] McMahon, P. L. The physics of optical computing. *Nature Reviews Physics* **5**, 717–734 (2023). 2308.00088.
- [26] Hamerly, R., Bernstein, L., Sludds, A., Soljačić, M. & Englund, D. Large-scale optical neural networks based on photoelectric multiplication. *Physical Review X* **9**, 021032 (2019).
- [27] Nerenberg, S., Neill, O., Marcucci, G. & Faccio, D. Photon number-resolving quantum reservoir computing. *arXiv preprint arXiv:2402.06339* (2024).
- [28] Gan, B. Y., Leykam, D. & Angelakis, D. G. Fock state-enhanced expressivity of quantum machine learning models. *EPJ Quantum Technology* **9**, 16 (2022).
- [29] Yin, Z. *et al.* Experimental quantum-enhanced kernels on a photonic processor. *arXiv preprint arXiv:2407.2036* (2024).
- [30] Ghosh, S., Paterek, T. & Liew, T. C. Quantum neuro-morphic platform for quantum state preparation. *Physical review letters* **123**, 260404 (2019).
- [31] Henaff, J. *et al.* Optical phase encoding in a pulsed approach to reservoir computing. *Optics Letters* **49**, 2097–2100 (2024).
- [32] Nokkala, J. *et al.* Gaussian states of continuous-variable quantum systems provide universal and versatile reservoir computing. *Communications Physics* **4**, 53 (2021).
- [33] Vandoorne, K. *et al.* Experimental demonstration of reservoir computing on a silicon photonics chip. *Nature communications* **5**, 3541 (2014).
- [34] Mujal, P. *et al.* Opportunities in quantum reservoir computing and extreme learning machines. *Advanced Quantum Technologies* **4**, 2102.11831.
- [35] Spagnolo, M. *et al.* Experimental photonic quantum memristor. *Nature Photonics* **16**, 318–323 (2022).
- [36] Li Deng. The MNIST database of handwritten digit images for machine learning research [best of the web]. *IEEE Signal Process. Mag.* **29**, 141–142 (2012).
- [37] Hochreiter, S. & Schmidhuber, J. Long short-term memory. *Neural Computation* **9**, 1735–1780 (1997).
- [38] Atiya, A. & Parlos, A. New results on recurrent network training: unifying the algorithms and accelerating convergence. *IEEE Trans. Neural Netw.* **11**, 697–709 (2000).
- [39] Govia, L. C. G., Ribeill, G. J., Rowlands, G. E. & Ohki, T. A. Nonlinear input transformations are ubiquitous in quantum reservoir computing. *Neuromorphic Computing and Engineering* **2**, 014008. 2107.00147.
- [40] Inubushi, M. & Yoshimura, K. Reservoir computing beyond memory-nonlinearity trade-off. *Sci Rep* **7**, 10199 (2017).
- [41] Akai-Kasaya, M. *et al.* Performance of reservoir computing in a random network of single-walled carbon nanotubes complexed with polyoxometalate. *Neuromorph. Comput. Eng.* **2**, 014003 (2022).
- [42] Fujii, K. & Nakajima, K. Harnessing disordered-ensemble quantum dynamics for machine learning. *Phys. Rev. Applied* **8**, 024030 (2017).
- [43] Fry, D., Deshmukh, A., Chen, S. Y.-C., Rastunkov, V. & Markov, V. Optimizing quantum noise-induced reservoir computing for nonlinear and chaotic time series prediction. *Sci Rep* **13**, 19326 (2023).
- [44] Clements, W. R., Humphreys, P. C., Metcalf, B. J., Kolthammer, W. S. & Walmsley, I. A. Optimal design for universal multiport interferometers. *Optica* **3**, 1460–1465 (2016).
- [45] Gattass, R. R. & Mazur, E. Femtosecond laser micromachining in transparent materials. *Nature photonics* **2**, 219–225 (2008).
- [46] Corrielli, G., Crespi, A. & Osellame, R. Femtosecond laser micromachining for integrated quantum photonics. *Nanophotonics* **10**, 3789–3812 (2021).
- [47] Ceccarelli, F. *et al.* Low Power Reconfigurability and Reduced Crosstalk in Integrated Photonic Circuits Fab-

- ricated by Femtosecond Laser Micromachining. *Laser & Photonics Reviews* **14**, 2000024 (2020).
- [48] Mood, A. M. Introduction to the theory of statistics. (1950).
- [49] Suprano, A. *et al.* Experimental property reconstruction in a photonic quantum extreme learning machine. *Physical Review Letters* **132**, 160802 (2024).
- [50] Cong, I., Choi, S. & Lukin, M. D. Quantum convolutional neural networks. *Nature Physics* **15**, 1273–1278 (2019).
- [51] Cimini, V. *et al.* Calibration of multiparameter sensors via machine learning at the single-photon level. *Physical Review Applied* **15**, 044003 (2021).
- [52] Carosini, L. *et al.* Programmable multiphoton quantum interference in a single spatial mode. *Science Advances* **10**, eadj0993 (2024).

Supplementary Material

I. PHOTONIC MEMRISTOR-BASED QUANTUM RESERVOIR COMPUTING

Reservoir computing is a supervised machine learning model that, given N_{tr} data points belonging to a training set $\{(x_k^{tr}, y_k^{tr})\}_{k=1}^{N_{tr}} \subset \mathbb{R}^n \times \mathbb{R}^m$, is supposed to find a target function $f_t: \mathbb{R}^n \rightarrow \mathbb{R}^m$, such that, $f_t(x_k^{train}) \simeq y_k^{train}$ for every k . Then, if the learning process is effective, the model should be able to generalize its operation to previously unseen data points $\{(x_k^{test}, y_k^{test})\}_k$, so that $f_t(x_k^{test}) \simeq y_k^{test}$. In general, this target function will not be linear and, in the reservoir computing case, it is given by the composition of two functions: $f(x) = W(g(x))$, where W is a linear functional, which acts on a non-linear function of the input x . The non-linear function is implemented by the dynamics of the reservoir (also equipped with memory). Then, the parameters of W are trained to minimize the distance between $W(g(x_k^{tr}))$ and y_k^{tr} . This last part of the algorithm amounts to a single layered artificial neural network.

In our work, we propose a quantum reservoir scheme, where the reservoir consists in a physical system, evolved through a quantum memristor. Then, this is followed by a classical artificial neural network, displaying only linear activation functions.

In order to investigate the feasibility and potentialities of the model, it is essential to study which kind of non-linearity we can achieve with a quantum memristor device. To this goal, let us consider a generic quantum state ρ , underlying a *completely positive trace preserving* (CPTP) map Λ . The evolved state is then measured through a Σ -output *positive operator-valued measure* (POVM), whose elements are indicate as E_m . In this context, the following mapping occurs:

$$\rho \rightarrow p_m = \text{Tr}(E_m \Lambda(\rho)) \quad (1)$$

and for $m \in (1, \dots, \Sigma)$, the output probability p_m is always linear in the elements of the density matrix of ρ [1]. However, by adding a feedback loop, the operation applied to the state ρ at time t_n , is affected (at least) by the output probability registered at time t_{n-1} . Indeed, in this case, the channel applied to the input state becomes a sequence of $\Lambda(t_n) = \Lambda(\rho(t_1), \dots, \rho(t_{n-1}))$, which depends on the states that were previously injected.

This implies then that, at time t_n , we will have:

$$\rho \rightarrow p_m(t_n) = \text{Tr}(E_m \Lambda(\rho(t_1), \dots, \rho(t_{n-1}))(\rho(t_n))) \propto \rho(t_1) \cdot \rho(t_2) \cdot \dots \cdot \rho(t_{n-1}) \quad (2)$$

This behaviour creates also an internal memory of previous states and such key features, non-linearity and memory, give the photonic quantum memristor the necessary ingredients for a reservoir computing model.

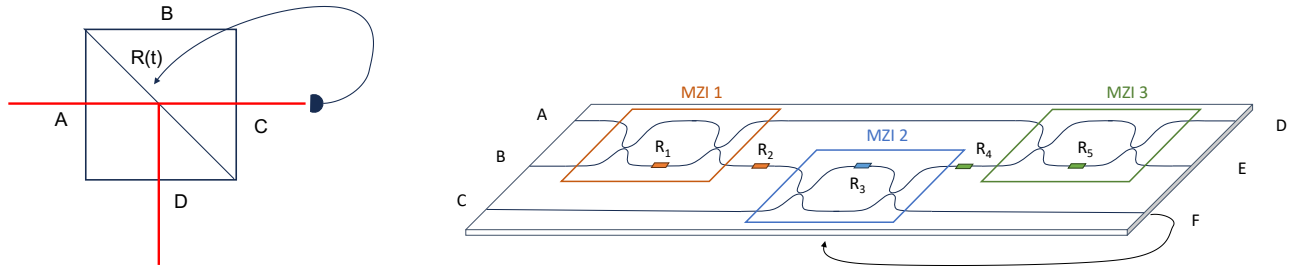


FIG. S1. **Quantum memristor schemes.** (a) **Original scheme for the quantum memristor.** This device is seen as a beam-splitter with a variable reflectivity, which is updated depending on the measurements performed on port C. In this configuration, the input state is a superposition of vacuum and a single photon state, injected into mode A, i.e. $\cos(\alpha)|0\rangle_A + \sin(\alpha)|1\rangle_A$. (b) **Quantum memristor integrated circuit.** In this case, the variable beam-splitter is replaced by a Mach-Zehnder interferometer (MZ2) and the input state is now encoded in the dual-rail encoding, as follows: $\cos(\alpha)|0\rangle_{AB} + \sin(\alpha)|1\rangle_{AB}$. This state, in the Fock basis, reads as $\cos(\alpha)|10\rangle_{AB} + \sin(\alpha)|01\rangle_{AB}$.

To test its effectivity, we apply our model to two tasks: first, the prediction of a non-linear function and, second, a time series prediction.

A. Non-linear function reproduction/prediction

For the first task, the functions we aim to reproduce are of the following kind:

$$f(x) = x^n, \quad n \in \mathbb{Z} \quad (3)$$

This choice is motivated by the interest in testing the achievable non-linear behaviour of our model and the role of the feedback loop of the quantum memristor towards its enhancement.

We encode the inputs as $x \rightarrow \sqrt{x}|0\rangle + \sqrt{1-x}|1\rangle$. To this end, we inject a photon from the lower input port of MZI1 of our photonic integrated platform (shown in Fig. S1b) and use a unitary U_{enc} to produce a coherent path superposition over the two modes A and B. In the Fock basis, this can be expressed as $x \rightarrow U_{enc}|0, 1\rangle_{AB} = \sqrt{x}|1, 0\rangle_{AB} + \sqrt{1-x}|0, 1\rangle_{AB}$. In this notation, 1 indicates the presence of a photon and 0 the vacuum state. However, since we use the so-called dual-rail encoding, we take $|1, 0\rangle_{AB} = |0\rangle$ and $|0, 1\rangle_{AB} = |1\rangle$.

Let us note that this encoding is linear when performing a projective measurement in the eigenvector basis of the Pauli operator σ_Z [2], as $Tr(\sigma_Z \rho_x) = \sum_{i=0,1} (-1)^i p_i = 2x - 1$, where p_i is the probability of getting outcome i . On the contrary, a measurement in the σ_X basis gives an expectation value that is non-linear in x , $Tr(\sigma_X \rho_x) = \sqrt{x}\sqrt{1-x}$. This non-linearity can be enhanced by rotating the state and choosing a proper measurement basis at the output. We indicate these two rotations U_1 and U_2 respectively, and perform them after the encoding (still through MZI1, which will implement $U_1 \cdot U_{enc}$) and before the measurement (through MZI3, which will implement $U_{meas} \cdot U_2$).

Then, to implement the quantum memristor, we add an ancillary spatial mode (C), and implement a unitary, U_{mem} , through MZI2, which acts on modes B and C (see Fig. S1b). Subsequently, the feedback rule modifies U_{mem} , with the update rule of the form $ap_F + c$, where p_F is the probability of detecting one photon coming out from output F. This modification can be defined, when we model the quantum memristor as a beam splitter with tunable reflectivity R (as in Fig. S1a), as:

$$R_t = \frac{1}{m} \sum_{T=t-m}^t R_T = \frac{1}{m} \sum_{T=t-m}^t (a^* p_{FT} + b^*) \quad (4)$$

where m is the memory extent of the model, i.e. the number of previous outcomes which directly affect the value $R(t)$. The relation between R and the internal phase of MZI2 (θ) is $R = \cos^2(\theta/2)$.

We consider then the rotations U_1 and U_2 , along with a and b , as optimizable hyperparameters.

More precisely, we minimize the following loss function: $p_D - x^n$ where p_D is the probability of detecting one photon coming out from mode D of the interferometer. This is done numerically, by using a gradient descent algorithm [3], in combination with *Adam* optimizer [4], with a learning rate of 0.4.

After finding the best hyperparameters, we run the experiment and feed the experimental statistics (i.e. a three-dimensional array containing the probabilities of detecting one photon on each output mode of the circuit) into the aforementioned artificial neural network, which is trained to perform the given task.

We performed the task also without any feedback loop, keeping the U_{mem} fixed, to compare the performance of the model in the two cases.

This comparison, with and without the memristor feedback loop, makes it possible to distinguish the contributions of encoding and feedback loop to the overall non-linearity. Let us note that, to have a fair comparison, we used hyperparameters that were separately optimized for these two models.

B. Non-linear Autoregressive Moving Average (NARMA) task

The goal of this task is to predict the output of the following non-linear dynamics [5, 6]:

$$y_{t+1} = 0.4y_t + 0.4y_t y_{t-1} + 0.6x_t^3 + 0.1, \quad (5)$$

where x_t and y_t indicate, respectively, the input and the output at time t . The input of the time series $\mathbf{x} = \{x_i\}_{i=1}^N$ is generated by sampling each x_i independently and uniformly in the interval $(0, \frac{1}{2})$ and, from Eq. (5), it is visible that the output y_{t+1} depends on past two outputs y_t and y_{t-1} as well as input x_t .

Analogously to the previous task (see section A), such an input sequence \mathbf{x} is encoded into a quantum state, through a unitary U_{enc} applied to a fixed state $|1\rangle$. In this case, the map is the following: $x_i \mapsto x_i|0\rangle + \sqrt{1-x_i^2}|1\rangle$. Then, the feedback rule to update the memristor reflectivity was chosen to follow the recursive equation

$$R_t = R_{t-1} + \frac{p_{(t-1)2} - R_{t-1}}{m}, \quad (6)$$

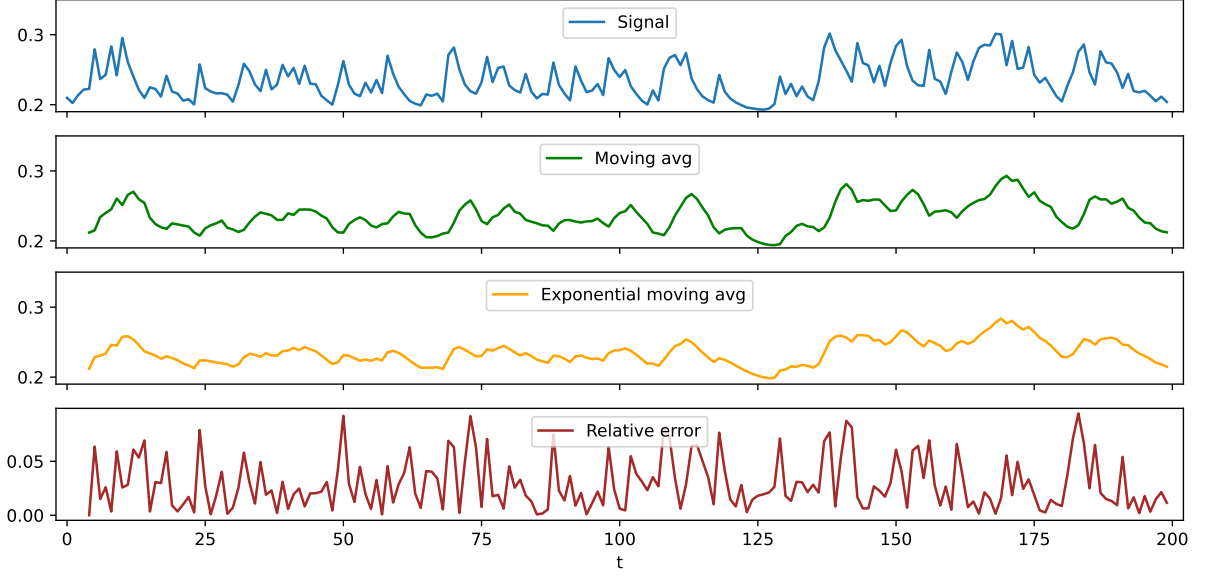


FIG. S2. **Feedback rules comparison.** Moving average (green) and exponential moving average (orange) on the NARMA task (blue) with sliding window of 4. The red line indicates the relative error between two averages in each point, which never exceeds 10%.

where p_{ti} is the probability of detecting one photon in the i -th mode ($i = D, E, F$), at time t , while $m \geq 1$ is the *extent of the memory* of the memristor, to which we also refer to as *sliding window* (see section C for further details). This update rule is called *exponential moving average* and, with respect to the one used for the previous task (see section A), it only remembers one previous data point. The comparison of these two feedback rules, that is, the moving average and exponential moving average, is shown in Fig. S2.

Solving the recursion equation in Eq. (6) yields:

$$R_t = \left(1 - \frac{1}{m}\right)^t \cdot R_0 + \frac{1}{m} \sum_{i=0}^{t-1} \left(1 - \frac{1}{m}\right)^i \cdot p_{t-i,2}, \quad (7)$$

where R_0 is the initial value of the reflectivity, which we set to $R_0 = \frac{1}{2}$ (balanced beam-splitter).

Let us note that the name *exponential moving average* comes from the fact that it amounts to a weighted moving average with exponentially decaying weights. Indeed, from Eq. (7), we can note that the memory of the initial condition and of the probabilities that are too far in the past, decay exponentially. This is convenient for the NARMA task, where the correlations between y_t and $y_{t-\tau}$ quickly disappear with increasing τ , as shown in Fig. S3. In the extreme cases, i.e. for $m = 1$ and $m \rightarrow \infty$, the memristor behaves as if it had no memory of previous inputs, i.e. $R(t) = p_{t,F}$, or with fixed behaviour where $R(t) \approx R(t-1)$.

The optimal trade-off value for m strongly depends on the task and can be treated as an hyperparameter. In our case, we chose $m = 4$, following the behaviour depicted in Fig. S3.

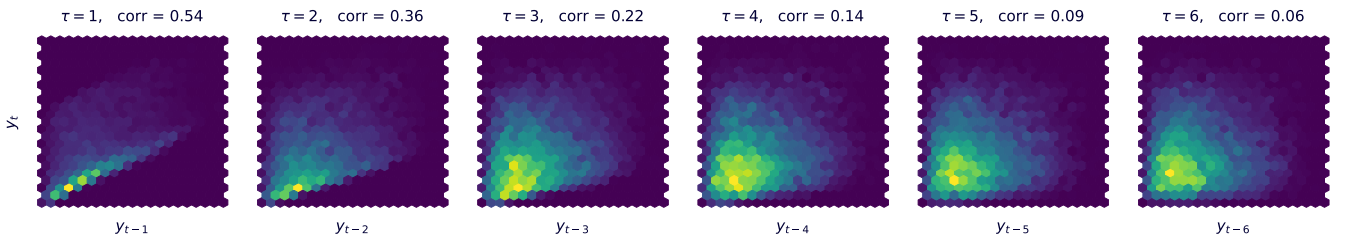


FIG. S3. **Consecutive output correlations in the NARMA task.** The plots show the correlations between y_t and $y_{t-\tau}$ for different time values (τ). The only significant correlations are up to $\tau = 3$. The numerical values for correlations at the top of each figure are Pearson correlation coefficient.

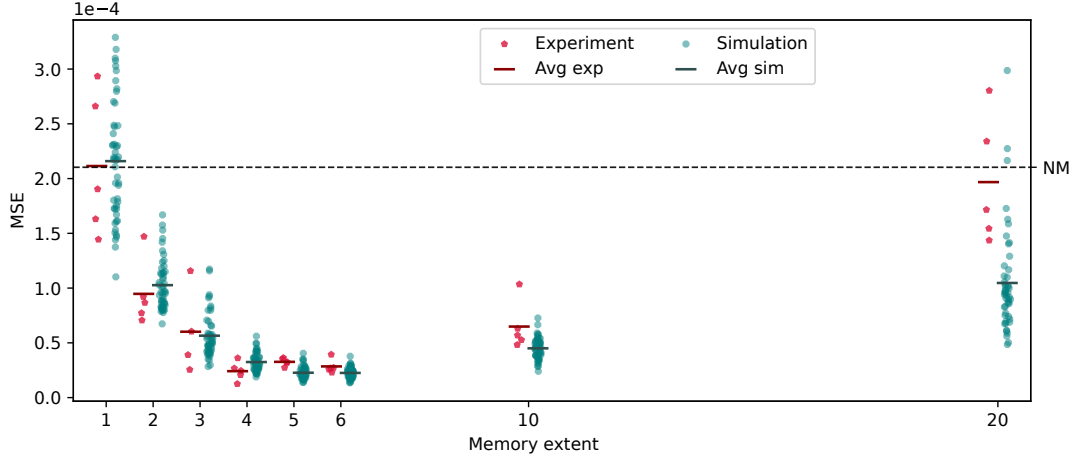


FIG. S4. **Mean squared error (MSE) for different memory extents in NARMA task.** We report the MSEs obtained from 50 (numerical) and 5 (experimental) runs with green and red polygons, respectively. The dark red and dark green lines indicate the average values. The average MSE gets lower with the increasing size of the sliding window (m) and it reaches its minimum at $\sim 2.5 \times 10^{-5}$ for $m = 6$. The dashed line (NM) indicates the case with no feedback loop.

In Fig. S4, we show the performance of the model for different sliding window parameters. Let us note that large values worsen the prediction, both in the numerical calculations and the experimental data. Indeed, for $N = 20$ the prediction from the experiment tends to be, on average, as good as the model without memory.

C. Comparison with classical models

In order to benchmark the performance of our quantum memristor-based reservoir computing scheme, we chose some models to compare it with. In detail, we picked the following three classes (in increasing complexity):

1. models without memory;
2. models with limited memory;
3. models with an *exponential average* memory.

Each class consists of a *linear* and *quadratic* models. In what follows, each model is described shortly:

1. **Models without memory.** These try to predict the next output of the network using **only** the last input to the network. The equation for this model is

$$y_{t+1} = \alpha u_t + \beta \quad \text{or} \quad y_{t+1} = \alpha u_t^2 + \beta u_t + \gamma$$

respectively for linear and quadratic models. The parameters α, β, γ are learnt during the training phase.

2. **Models with limited memory.** These have additional access to the previous input point. The model then takes the form:

$$y_{t+1} = \alpha u_t + \beta u_{t-1} + \gamma \quad \text{or} \quad y_{t+1} = \alpha u_t^2 + \beta u_{t-1} + \gamma,$$

respectively, for linear and quadratic model. The parameters α, β, γ are learnt during the training phase.

3. **Model with *exponential moving average* memory.** These models have access to the exponential moving average with an extent of memory of 4, which is the closest comparable case to the network with the quantum memristor. The equation of that model is

$$y_{t+1} = \alpha u_t + \text{Exp}(u_t, 4) + \gamma \quad \text{or} \quad y_{t+1} = \alpha u_t^2 + \text{Exp}(u_t, 4) + \gamma,$$

respectively, for the linear and quadratic model, where

$$\text{Exp}(u_t, \tau) := \left(1 - \frac{1}{\tau}\right)^t \cdot \frac{1}{4} + \frac{1}{\tau} \sum_{i=0}^{t-1} \left(1 - \frac{1}{\tau}\right)^i \cdot x_{t-i}$$

is the equation for exponential moving average, which is exactly Eq. (7) with $R_0 = \frac{1}{4}$ (let us note that this initial value has no influence on the predictions after the washout points).

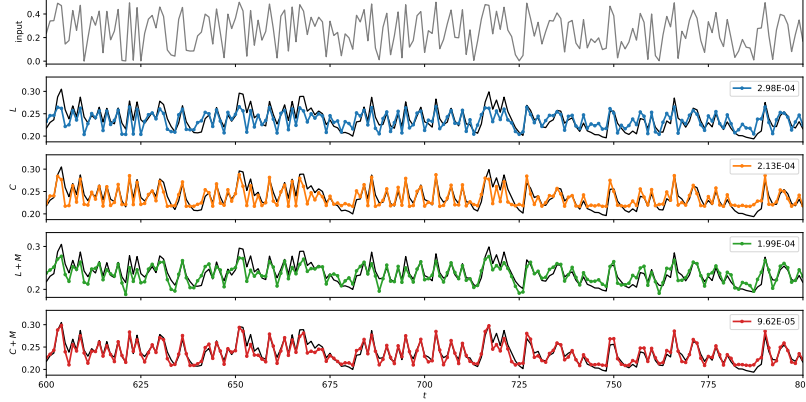


FIG. S5. **Performance of different learning models on NARMA task.** The plot shows the prediction of the chosen three classes of classical models on the NARMA task. In detail, L and Q indicate a model with no memory which can manipulate the input, respectively, linearly and quadratically. $L + M$ and $Q + M$ indicate a model which can manipulate the input, respectively, linearly and quadratically and have access to the previous outcome of the model. L^M and Q^M indicate a model which can manipulate the input, respectively, linearly and quadratically and have access to the exponential average of the last 4 outcomes. All models are trained on the same dataset of length 1000. The first 20 data points are used to washout the memory, the following 480 points for training and the remaining 500 for testing. For the sake of clarity, we display only 200 points from the test dataset.

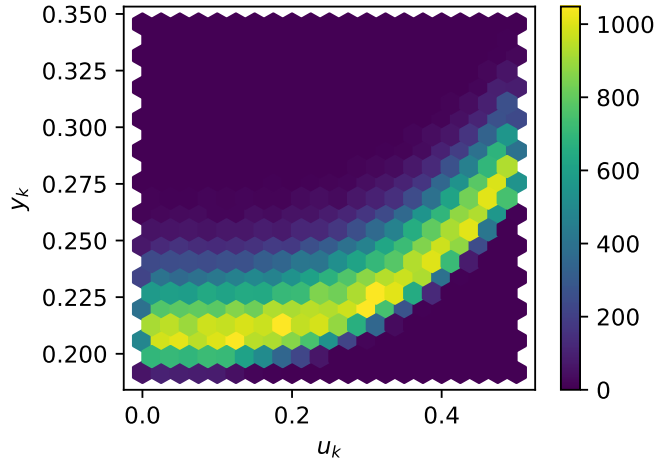


FIG. S6. **Input/output relation for NARMA task.** The plot shows that the non-linearity of the NARMA task is not very high, for inputs between 0 and 0.5. This explains why also the considered linear models have reasonably good performances on this task.

The behaviour of the models on an example dataset can be seen in the Fig. S5. Let us note that also linear models with limited memory have a good performance, due to the low non-linearity of the NARMA task, which is highlighted in Fig. S6.

II. ON-CHIP QUANTUM TOMOGRAPHY OF QUANTUM MEMRISTOR OUTPUT STATE

As detailed in [7] and in the main text, the photonic quantum memristor has two features: (i) *memristive behaviour* and (ii) *quantum coherent processing*. These characteristics seem in contradiction, as the evolution of closed quantum systems is intrinsically linear, while open systems have low coherence. However, the weak measurement scheme implemented by our device allows to express non-linear behavior, while preserving some coherence.

Let us consider the original scheme of the photonic quantum memristor (see Fig. S1a), namely a beam splitter with variable reflectivity, where we inject a coherent superposition of vacuum and a single photon state into input mode A, i.e. $\cos(\alpha)|0\rangle_A + e^{(i\phi)}\sin(\alpha)|1\rangle_A$. Then, one of the two output modes (C), is measured and the reflectivity of the beam splitter is varied according to a feedback loop.

In our case, we simulate this input state, using the circuit in Fig. S1b, where we use the first two spatial modes (A and B) to encode a qubit state, with dual rail encoding, i.e. $\cos(\alpha)|0\rangle + e^{(i\phi)}\sin(\alpha)|1\rangle$. For convenience, we will express this state in terms of occupational numbers, i.e. $\cos(\alpha)|10\rangle_{AB} + e^{(i\phi)}\sin(\alpha)|01\rangle_{AB}$. Then, we place a variable beam splitter, i.e. a Mach-Zehnder interferometer, acting between modes B and C (MZI2). The state will evolve then as follows:

$$\begin{aligned} \rho_{out} = & |\cos(\alpha)|^2|100\rangle_{DEF}\langle 100| + \cos(\alpha)\sin(\alpha)e^{-i\phi}\sqrt{1-R}|100\rangle_{DEF}\langle 010| - \\ & i\cos(\alpha)\sin(\alpha)e^{-i\phi}\sqrt{R}|100\rangle_{DEF}\langle 001| + \\ & \cos(\alpha)\sin(\alpha)\sqrt{1-R}|010\rangle_{DEF}\langle 100| + |\sin(\alpha)|^2(1-R)|010\rangle_{DEF}\langle 010| - \\ & i|\sin(\alpha)|^2\sqrt{R(1-R)}|010\rangle_{DEF}\langle 001| + \\ & i\cos(\alpha)\sin(\alpha)\sqrt{R}|001\rangle_{DEF}\langle 100| + i|\sin(\alpha)|^2\sqrt{R(1-R)}|001\rangle_{DEF}\langle 010| + \\ & |\sin(\alpha)|^2R|001\rangle_{DEF}\langle 001| \end{aligned} \quad (8)$$

where R is the reflectivity of the beam splitter (corresponding to $\cos^2(\frac{\theta}{2})$), if we consider the internal phase of MZI2).

At this point, we want to quantify the coherence of the output state of the memristor, tracing out the part used for the feedback loop. Namely, we are interested in the state coming out of the first two modes of the circuit in Fig. S1b, D and E, or, analogously from port D of Fig. S1a. To do this, we trace out mode F and obtain the following state:

$$\begin{aligned} \rho_{out} = & |\cos(\alpha)|^2|10\rangle_{DE}\langle 10| + \\ & |\sin(\alpha)|^2(1-R)|01\rangle_{DE}\langle 01| + \\ & |\sin(\alpha)|^2R|00\rangle_{DE}\langle 00| + \\ & \cos(\alpha)\sin(\alpha)e^{-i\phi}\sqrt{1-R}|10\rangle_{DE}\langle 01| + \\ & \cos(\alpha)\sin(\alpha)\sqrt{1-R}|01\rangle_{DE}\langle 10| \end{aligned} \quad (9)$$

To be consistent with the original scheme of the quantum memristor, we must note that the two states $|10\rangle_{DE}$ and $|00\rangle_{DE}$ both correspond to the state $|0\rangle_D$ of the original scheme (see, respectively, Fig. S1a and Fig. S1b). Indeed, both states correspond to vacuum at the non-measured output of MZI2. Hence, the density matrix is the following:

$$\begin{aligned} \rho_{out}^* = & |\cos(\alpha)|^2|0\rangle\langle 0| + \\ & |\sin(\alpha)|^2(1-R)|1\rangle\langle 1| + \\ & |\sin(\alpha)|^2R|0\rangle\langle 0| + \\ & \cos(\alpha)\sin(\alpha)e^{-i\phi}\sqrt{1-R}|0\rangle\langle 1| + \\ & \cos(\alpha)\sin(\alpha)\sqrt{1-R}|1\rangle\langle 0| \end{aligned} \quad (10)$$

The purity of this state is then:

$$Tr(\rho_{out}^{*2}) = 1 - 2\sin(\alpha)^4R(1-R) \quad (11)$$

From Eq. (11), we note that the output state is pure, when the reflectivity is either 0 or 1. Indeed in the extremal case when $R = 0$, the input remains unchanged, as the memristor performs the identity transformation. Instead, when $R = 1$, the portion of the state that goes in the memristor is completely redirected to the measured mode F

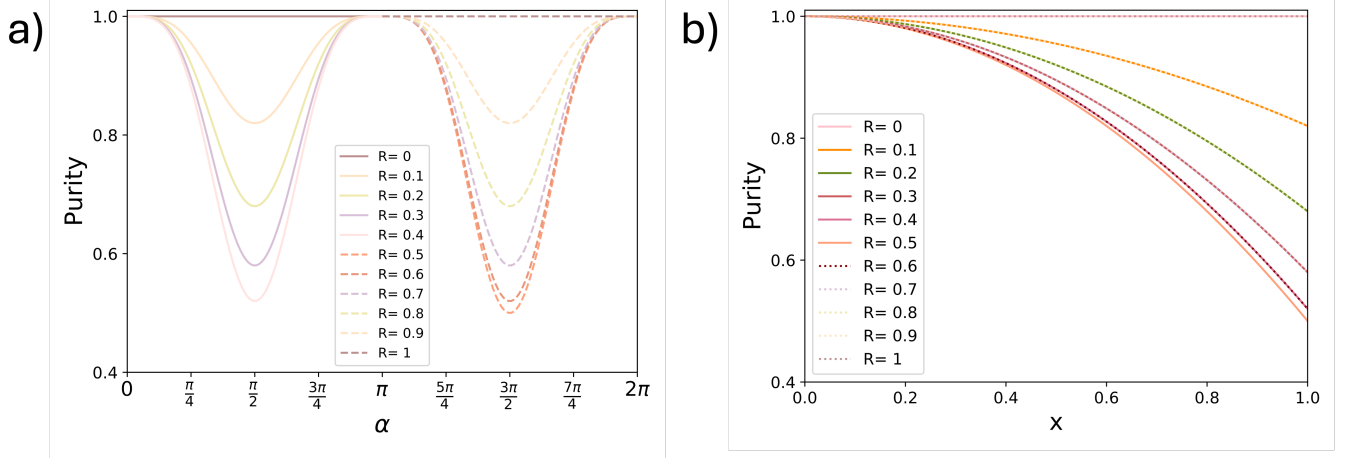


FIG. S7. **Partial output state purity.** (a) Purity dependence on the α parameter, considering the input state as $\cos(\alpha)|10\rangle_{AB} + \sin(\alpha)|01\rangle_{AB}$. The behavior is shown for different values of R and, as expected, it is periodic with an interval of π . For the sake of clarity, for $R \geq 0.5$, the behaviour is shown in the interval from π to 2π with dashed curves. Note that, for reflectivities $R = r$ and $R = 1 - r$, e.g. $R = 0.1$ and $R = 0.9$, the curves overlap. The lowest purity is obtained for $R = 0.5$ and $|\sin(\alpha)| = 1$ (i.e. $\alpha = \frac{\pi}{2} + i \times \pi$, for $i = 0, 1, \dots$), as it can be derived from Eq. (11). (b) We show the same behaviour as in the previous plot, but considering our classical data encoding, i.e. $\sqrt{1-x}|1, 0\rangle_{AB} + \sqrt{x}|0, 1\rangle_{AB}$. For values $R \leq 0.5$ we use solid lines and, for $R > 0.5$, dashed lines, to show the overlap for reflectivities $R = r$ and $R = 1 - r$, e.g. $R = 0.1$ and $R = 0.9$. Also in this case, it is visible that the lowest purity is displayed for $|x| = 1$ and $R = 0.5$ (see Eq. (13)).

(or C). Hence, when tracing it out and looking only at the other output mode of the beam splitter/MZI, the only detected state is vacuum. The expected values of the purity for different reflectivities and input states (i.e. α) are shown in Fig. S7. Let us note that, due to the symmetric form of Eq. (11), the curves for reflectivities R and $1 - R$ overlap.

Experimentally, we evaluated the purity for three different input states $\sqrt{1-x}|0\rangle + \sqrt{x}|1\rangle$ (with $x = 0.1, 0.5, 0.9$) and three values of R . To this aim, we performed a quantum state tomography on the output state in modes D and E of the circuit, exploiting MZI1 for the encoding MZI3 for the measurements. MZI2 was used to select the reflectivity (see Fig. S1b).

From a practical point of view, to produce each state $\sqrt{1-x}|0\rangle + \sqrt{x}|1\rangle$ and reflectivity R , we injected a single photon from mode B of our circuit and set the internal phase of MZI1 to $2 \times \arccos(\sqrt{1-x})$ and MZI2 as $2 \times \arccos(\sqrt{R})$. Then, to perform the quantum state tomography, we implemented projective measurements onto the Pauli operators bases, i.e. σ_x , σ_y and σ_z . The corresponding internal/external phases (ϕ/ψ) for MZI3 were, respectively, $(0/\frac{\pi}{2})$, for σ_x , $(\frac{\pi}{2}/\frac{\pi}{2})$, for σ_y and $(0/0)$, for σ_z .

The resulting experimental density matrices are shown in Fig. S8. The expected ones (ρ_{exp}), instead, are shown in Fig. S9. In the Fock notation, ρ_{exp} amounts to:

$x = 0.1$	$R = 0$	$R = 0.5$	$R = 1$	$x = 0.5$	$R = 0$	$R = 0.5$	$R = 1$
$Tr(\rho_{out}^{*2} exp)$	1.00	0.95	0.99	$Tr(\rho_{out}^{*2} exp)$	0.96	0.82	0.98
$Tr(\rho_{out}^{*2} th)$	1.00	0.99	1.00	$Tr(\rho_{out}^{*2} th)$	1.00	0.87	1.00
$x = 0.9$	$R = 0$	$R = 0.5$	$R = 1$				
$Tr(\rho_{out}^{*2} exp)$	0.93	0.61	0.99				
$Tr(\rho_{out}^{*2} th)$	1.00	0.59	1.00				

TABLE S1. **Experimental purity on partial output state.** We show the values obtained experimentally, from the reconstructed density matrix of the output state ρ_{DE} , when tracing out the mode used for the feedback loop (F). These values are then compared to the expected ones, obtained through Eq. (13).

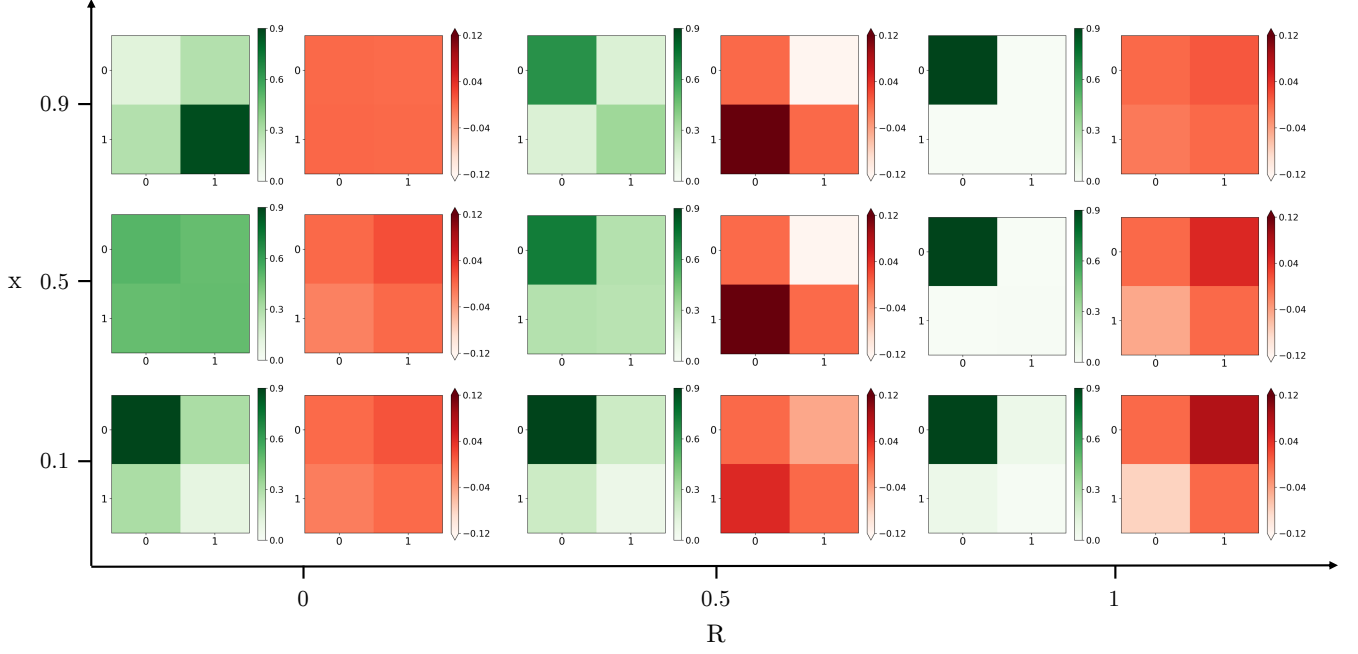


FIG. S8. **Experimental density matrix of the memristor partial output state.** We performed the quantum state tomography on the state exiting from the first two modes of our circuit (D and E), for several values of the reflectivity of the memristor, i.e. $R = 0, 0.5, 1$, and input states $\sqrt{1-x}|1,0\rangle_{AB} + \sqrt{x}|0,1\rangle_{AB}$, i.e. $x = 0.1, 0.5, 0.9$. In green, we show the colourplot of the real part of the experimental density matrix, while, in orange, the imaginary part. Let us note that, on the element $|0\rangle\langle 0|$ we manually added the term $x_{exp}^2 R = p_F$, to be consistent with the original model of the quantum memristor.

$$\begin{aligned}
 \rho_{exp} = & x|10\rangle\langle 10| + \\
 & (1-x)(1-R)|01\rangle\langle 01| + \\
 & \sqrt{x(1-x)}e^{-i\phi}\sqrt{1-R}|10\rangle\langle 01| + \\
 & \sqrt{x(1-x)}\sqrt{1-R}|01\rangle\langle 10|
 \end{aligned} \tag{12}$$

Let us note that, since we post-select events where we detect one photon, either on output mode D or E, the term $x^2 R|00\rangle\langle 00|$ is not directly measured in the tomography. Hence, to retrieve the purity, we evaluated the experimental value of x (x_{exp}) from the density matrix and then applied to Eq. (11), which now reads as:

$$Tr(\rho_{out}^{*2}) = 1 - 2x_{exp}^2 R(1-R) \tag{13}$$

The experimental purity values, together with the expected ones, are reported in Table S1.

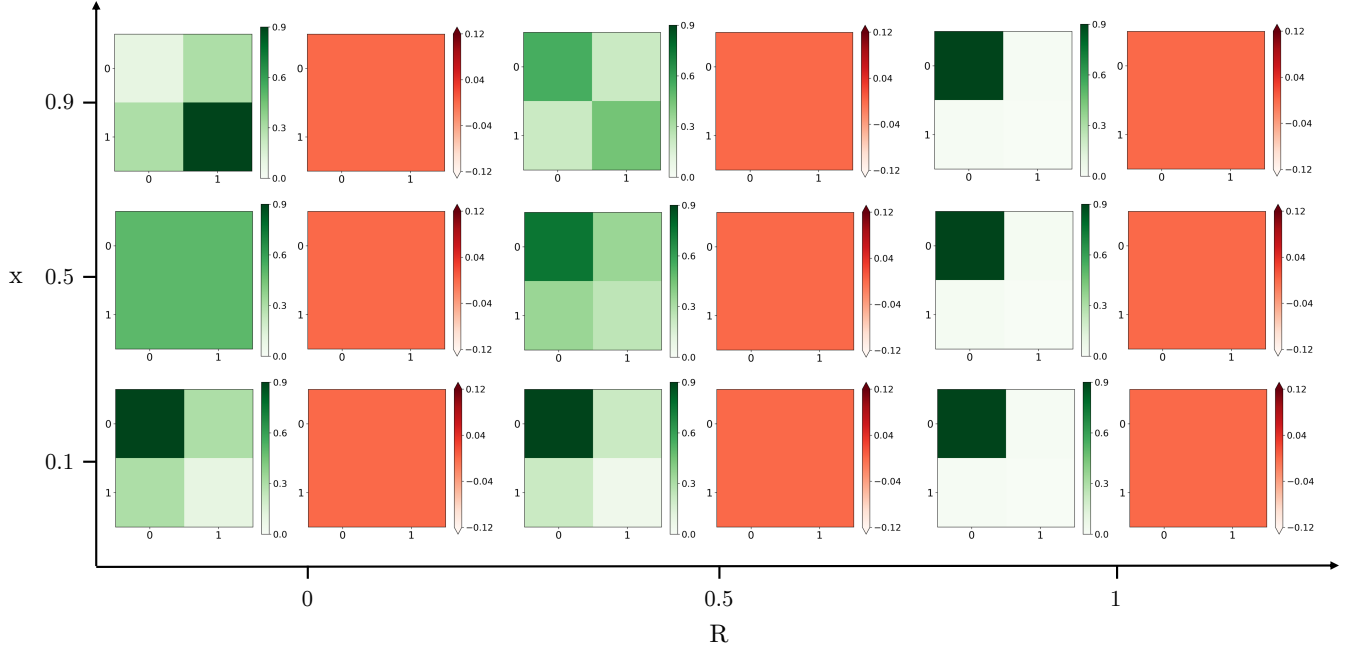


FIG. S9. **Expected density matrix of the memristor partial output state.** We consider the memristor output state, tracing out mode F, for several values of the reflectivity of the memristor, i.e. $R = 0, 0.5, 1$, and input states $\sqrt{1-x}|1, 0\rangle_{AB} + \sqrt{x}|0, 1\rangle_{AB}$, i.e. $x = 0.1, 0.5, 0.9$. In green, we show the colourplot of the real part of its density matrix, while, in orange, the imaginary part.

-
- [1] Innocenti, L. *et al.* Potential and limitations of quantum extreme learning machines. *Communications Physics* **2023** 6:1 **6**, 1–9 (2023).
 - [2] Govia, L. C. G., Ribeill, G. J., Rowlands, G. E. & Ohki, T. A. Nonlinear input transformations are ubiquitous in quantum reservoir computing. *Neuromorphic Computing and Engineering* **2**, 014008. 2107.00147.
 - [3] Ruder, S. An overview of gradient descent optimization algorithms. *arXiv preprint arXiv:1609.04747* (2016).
 - [4] Diederik, P. K. Adam: A method for stochastic optimization. *Proceedings of the 3rd International Conference for Learning Representations, San Diego, 2015* (2015).
 - [5] Atiya, A. & Parlos, A. New results on recurrent network training: unifying the algorithms and accelerating convergence. *IEEE Trans. Neural Netw.* **11**, 697–709 (2000).
 - [6] Hochreiter, S. & Schmidhuber, J. Long short-term memory. *Neural Computation* **9**, 1735–1780 (1997).
 - [7] Spagnolo, M. *et al.* Experimental photonic quantum memristor. *Nature Photonics* **16**, 318–323 (2022).